Fault slip envelope: A new parametric investigation tool for fault slip based on geomechanics and 3D fault geometry

Roger Soliva[1], Frantz Maerten[2], Laurent Maerten[3], Jussi Mattila[4]

[1]Geosciences Montpellier, Université de Montpellier, Campus Triolet, CC060, Place Eugène Bataillon, 34095 Montpellier Cedex 05, France. *roger.soliva@umontpellier.fr*

[2]Youwol, France. *fmaerten@youwol.com*

[3]Schlumberger, 340 rue Louis Pasteur, 34790 Grabels, France. *lmaerten@slb.com*

[4]Geological Survey of Finland, P.O. Box 96, 02151 Espoo, Finland. *jussi.mattila@gtk.fi*

Correspondence to: Roger Soliva (*roger.soliva@umontpellier.fr*)

Abstract

By combining 3D boundary element model, frictional slip theory and fast computation method, we propose a new tool to improve fault slip analysis that allows to analyze a very large number of scenarios of stress and fault mechanical properties variations through space and time. Using both synthetic and real fault system geometries we analyze a very large number of numerical simulations (125,000) using fast iterative method to define for the first time macroscopic rupture envelopes for fault systems, referred to as "fault slip envelopes". Fault slip envelopes are defined using variable friction, cohesion and stress state, and their shape is directly related to the fault system 3D geometry and the friction coefficient on fault surfaces. The obtained fault slip envelopes shows that very complex fault geometry implies low and isotropic strength of the fault system compared to geometry having limited fault orientations relative to the remote stresses, providing strong strength anisotropy. This technique is applied to the realistic geological conditions of the Olkiluoto high-level nuclear waste repository (Finland). The model results

suggests that Olkiluoto fault system has a better ability to slip under the present day Andersonian thrust stress regime, than for the strike-slip and normal stress regimes expected in the future due to the probable presence of an ice sheet. This new tool allows to quantify the anisotropy of strength of 3D real fault networks as a function of a wide range of possible geological conditions and mechanical properties. This can be useful to define the most conservative fault slip hazard case or to account for potential uncertainties in the input data for slip. This technique therefore applies to earthquakes hazard studies, geological storage, geothermal resources along faults and fault leaks/seals in geological reservoirs.

1 Introduction

Better understanding of the mechanical interplay between fault slip, 3-D fault geometry, stresses, and rock mechanical properties (e.g. Byerlee, 1978; Morris and Ferril, 1996; Lisle and Srivastava, 2004; Moeck et al., 2009) is an actual and future scientific challenge in geosciences because (1) conventional failure or plasticity laws derived from rock testing does not apply to large rock volumes at geological conditions and time scale (e.g. Brantut et al., 2013), and (2) because fault slip has increasing societal applications (e.g. slip hazard, seismicity, hydraulic fracturing, fault mechanical seal, rock stability, unconventional resources and storage of gas, CO_2 and compressed air).

Although the general knowledge on the geometry, constitution and the behavior of fault zones is improving (e.g. Holdsworth, 2004; Faulkner et al., 2006; Wibberley et al., 2008), it is clear that the large-scale strength of a faulted rock volume is poorly known (e.g. Colettini et al., 2009; McLaskey et al., 2012). Laboratory tests on sampled rocks or fault rocks partly resolve this problem in giving a range of mechanical properties and friction laws. The strength of rocks has been classified under several types of behavior defined by rupture or plasticity envelopes with respect to rock type (Mohr Coulomb, Byerlee, Griffith, Cam Clay types), which describe typically the elastic domains of small, intact or precut rock samples (Byerlee, 1978; Rutter and Glover, 2012). For pre-existing fault surfaces, fault stability is generally described by the Mohr-Coulomb theory, in which the shear strength (τ) of a fault surface depends on the amount of static friction (μ), the normal stress (σ_n) and cohesion (C_o) on this surface (e.g. Scholz, 2019):

2

$$\tau = \mu\sigma_n + C_o \qquad\qquad (1)$$

On a simple-planar fault surface, static friction and cohesion define the deviatoric and normal stresses to be applied for fault reactivation (Byerlee, 1978), here referred to as "fault slip". However, as the result of multi-stage plate tectonic motions and rock heterogeneity in the Earth's crust, both intra- in inter-plate crustal rocks are affected by multiple fracture and fault systems able to slip (e.g. Townend and Zoback, 2000; Anderson et al., 2003), which are more or less complex in their organization on a wide range of scales (isolated, segmented, listric, restricted, branching, intersecting, e.g. Marrett and Almendinger, 1990; Nicol et al., 1996; Karlstrom and Williams, 1998; Kattenhorn and Pollard, 2001; Soliva et al., 2008). Realistic geometries of faults necessarily imply variations of the shear and normal stresses resolved on the fault surfaces and consequent anisotropy of strength. This concerns the strength of potentially large rock volumes containing faults, governed by their 3D geometry, stress state and frictional behavior, for which the value and anisotropy of strength is still a challenge to quantify.

Slip tendency analysis is a well-known method providing tools considering the ratio of resolved shear to normal stresses to model the likelihood for slip on pre-existing surfaces of all possible orientations relative to a regional stress field (e.g. Arthaud, 1969; Morris et al., 1996; Lisle and Srivastava, 2004; Collettini and Trippetta, 2007; Lejri et al., 2017). Beyond its successful application to many cases of fault slip hazard or induced seismicity (e.g. Moeck et al., 2009, Yukutake et al., 2015), this method does not provide the possibility to analyze together large number of geological conditions such as variations of stress state, orientation, friction, cohesion or fluid pressure. Fault slip hazard has generally to be analyzed thoroughly with respect to potential variation through space and time of such important parameters, which actually requires full and time-consuming parametric modeling, and therefore fast calculation techniques. Such a development is however critically needed in the new age of data science and numerical geology featured by an increasing availability of 3D-numerical fault system data, in situ rock properties, stress measurements, and high-speed computers. It is also a way to account for potential uncertainties in the input data and to define the most conservative fault slip hazard case.

An improvement of the slip tendency analysis tool or other equivalent numerical method (Neves et al., 2009; Alvarez del Castillo et al, 2017), would be to combine 3D mechanical model, allowing to analyse DFN (discrete fault or fracture network) subjected to multiple cases of stress states, and in which fault strength is resolved

using a complete static frictional behavior (including cohesion). Although well accepted, Mohr Coulomb's theory

has been recently regarded more critically to explain fault initiation under polyaxial loading or in situations where

sigma 2 is not parallel to a pre-existing fault (Healy et al., 2015; Hackston and Rutter, 2016). This fault initiation

process, which probably relies more on 3D stress perturbation around the first initiated faults or pre-existing defect

(e.g. Crider and Pollard, 1998; Kattenhorn et al., 1999; Maerten et al., 2002; also see Olson, 1993, for a critical

analysis of the Coulombs theory for fault initiation), does not discredit the applicability of the Coulomb's theory on

reactivation of pre-existing fault surface and stress magnitude at failure (Reches, 1983). It can however justify the

need to consider friction as a potential variable in a wider range than provided by common triaxial test data. Any

attempt to quantify the strength of fault systems therefore depends on the development of models coupling pre-

existing 3D fault geometry with both variable fault mechanical properties and triaxial loading conditions through

space and time.

In this paper, we use a 3D boundary element numerical model (Ibem3D, e.g. Maerten et al., 2014) in which

a Coulomb's frictional law is resolved on DFN surfaces to quantify fault system static strength as a function of

variable mechanical parameters in a range consistent with geological conditions, and to assess zones having

potential for fault slip. Using fast calculation iterative method allowing to analyze a very large number of numerical

simulations (125,000), we define macroscopic fault slip envelopes of rock volumes containing faults as a function of

variable stress orientation, 3D faults geometry and frictional properties. This technique, applied to the case study of

the Olkiluoto fault system, allows analyzing fault-slip hazard for multiple geological scenarios, including variable

triaxial stress profiles through space and time, and fault mechanical properties in the range of potential uncertainties

derived from mechanical tests.

2 Method

2.1 Fault slip envelope setup

We propose to calculate fault slip envelopes for both synthetic and real fault system geometry using the 3D

numerical model iBem3D, a quasi-static iterative Boundary Element Model (Maerten et al., 2014). In iBem3D,

faults are discretized using triangulated surfaces of frictional behavior (Eq. 1) in a heterogeneous, isotropic elastic

whole- or half-space also allowing mechanical interaction between each triangular element when the fault surfaces

slip (Maerten et al., 2002). For the first part of this study aiming to define fault slip envelopes, the effective stress

state is simplified as a horizontal, simple-uniaxial stress (σ) of 10 MPa with variation of the angle $\theta \in [0, 180°]$ with respect to fault orientation. This uniaxial condition allows highlighting the dependence of fault slip on friction and cohesion under simple stress condition. Modeling using more realistic stress conditions (i.e. in 3D and evolving with space and time) will be used for the Olkiluotto fault system study (see section 2.2). Static friction and cohesion values, as measured in laboratory rocks tests or from deep stress measurements, typically vary in the range of $\mu \in [0, 1]$ and $C_0 \in [0, 10]$ MPa, respectively (Hatheway and Kiersch, 1989). To analyse the sensitivity of fault slip as a function of these properties and stress orientation (μ, C_0 and θ), we use them as variables in the given ranges, with 50 values for each parameter. This leads to the analysis of a very large number of models (50^3 = 125,000). The computation time has therefore been optimized using H-Matrix technique parallelized for multi-core CPU architectures. The resulting fault slip envelope separates the parametric domain (μ, C_0 and θ) in which the fault is unstable (slip) from which the fault is stable (no slip). Also note that fluid pressure, although not considered in this study (see section 4), is considered in iBem3D as an isotropic pressure into the faults that can also be considered as a variable.

Fault slip can occur in places where the Coulomb's criterion is reached on fault surfaces. In other words, slip occurs along preferred orientations of fault surfaces with respect to the amount of friction, cohesion and resolved shear and normal stresses on fault planes computed following the Cauchy equations (e.g. Pollard and Fletcher, 2005; Jeager and Cook, 1989). Quasi-static fault displacement (net slip) can be computed on fault planes using linear elasticity (see Thomas, 1993; Maerten et al., 2010; 2014; 2018 for full explanation), taking into account static friction and cohesion, mechanical interaction due to stress perturbation between faults (e.g. Crider and Pollard, 1998; Kattenhorn et al, 2000; Soliva et al., 2008; Maerten et al., 2014), and using Young's modulus (E) and Poisson's ratio (ν) of value 1 GPa and 0.25, respectively. This quasi-static displacement, rather than the coseismic value of displacement which must also be affected by dynamic rupture processes, is considered as the fault ability to initiate and accumulate slip along fault.

We studied first a synthetic fault geometry characterized by a 60° dip simple-planar elliptical surface such as described for a simple-isolated normal fault (Nicol et al., 1996, Figure 1a). More complex synthetic geometries were also tested, such as intersecting conjugate faults, consistent with normal (60° dip), strike-slip (90° dip), thrust-fault configurations (30° dip), a more complex pattern containing all these configurations (Figure 2a), or again the case of the sphere (Figure 2b). Fault slip envelopes have also been calculated on the three real fault system

135   geometries (or DFN) shown in Figure 3a, b and c: Landers, Chimney Rock and Oseberg Syd, respectively, used in

Maerten et al. (2001), Maerten et al. (2002), Lovely et al. (2009) and Madden et al. (2013). For the Landers and

Chimney Rock cases, the 3D faults surfaces were extruded downward from a 2D trace mapped at the Earth's

surface, whereas the Oseberg Syd geometry is derived from high quality seismic reflexion survey. Uncertainty about

3D fault geometry discretization is not accounted for in this study (see the discussion in section 4). For these 3 fault

140   system configurations, the uniaxial stress orientation $\theta = 0°$ corresponds to the West, $\theta = 90°$ to the North and $\theta =$

180° to the East. The aim is therefore not to provide a geologically plausible study (as exposed in section 2.2 for the

Olkiluoto fault system study), but to illustrate fault slip envelope as a function of fault system complexity using

realistic fault geometry.

145   **2.2 Parametric study of the Olkiluoto fault system**

We apply this technique to study the potential of fault reactivation in the fault system of Olkiluoto Island

(Finland), where a deep geological high-level nuclear waste repository is being built and which also is a site for two

operational nuclear power plants. The site is located in Paleoproterozoic amphibolite-facies metasedimentary rocks

and tonalitic-granodioritic-granitic gneisses, cut by a complex 3D geometry of brittle faults, spanning in age from

150   1.7 to 1.0 Ga and formed during several different tectonic episodes (Mattila and Viola, 2014). It is thought that these

faults may be subjected to reactivation in a future glacial cycle (120 kyrs from now) due to the loading-unloading

effect of a glacial ice sheet cover. Such an event is evidenced by prominent post-glacial faults observed in northern

Scandinavia, known to have occurred at the retreating phase of the last glaciation (Arvidsson, 1993). The stress state

evolution due to this ice sheet cover is expected to be the major change in loading conditions of the fault system

155   surrounding the Olkiluoto site and northern Europe in general.

The present day stress state (Figure 6a, 0 m of ice), the 3D shape of this fault system (Figure 6b), and the

rock mechanical properties have been thoroughly inspected in the area from the 1980's to present day and are used

to constrain our modeling. The DFN geometry has been defined by 3D and 2D seismic surveys and cross-hole data

correlation of a total of 57 diamond-cored boreholes and the underground characterization facility, reaching the

160   depth of 450 m (Aaltonen et al., 2010). This fault system, which extends at least to the depth of 2 km, is used in our

simulation as a relevant example of real 3D fault system complexity in a highly important area. A fine discretization

of the fault surfaces with triangular elements representing less than hundred meters in length allows the use of high-

accuracy fault geometry as required to study fault slip and mechanical interaction.

Based on present day stresses (σ_H is E-W) and elastic rock properties ($E = 55$ GPa and $\nu = 0.25$) (see additional material and Sjöberg, 2003; Hakkala et al., 2013) we approximate realistic stress boundary-conditions in considering the presence of the next future-glacial ice sheet. Because in geological conditions principal stress axes are subjected to permutations through time and space, such an approach gives the opportunity to see geologically consistent effects of changing stress magnitudes, Andersonian regime (i.e. $\sigma_v = \sigma_1$, $\sigma_v = \sigma_2$ or $\sigma_v = \sigma_3$) and the relative angle between the stresses and the faults (θ). Since lithosphere flexural stresses or stress earthquake triggering are difficult to define, it is worth considering principal stresses as variable parameters in a lower end-member case scenario. The presence of an ice sheet in the area will at least increase the vertical load due to its increase of thickness. Based on climate models and previous studies of the past glacial events (Skinner and Porter, 1987; Berger and Loutre, 1997), the ice sheet is expected to vary from 0 up to 2.5 km thickness above the faults during the next 120 kyrs, with a maximum thickness reached at 100 kyrs from nowadays. The subsequent stress state into the rock mass is calculated from the measured present day stress field (overcoring and hydraulic fracturing, Ask, 2011) and additional vertical and confining stresses due to the ice thickness.

We calculated the triaxial stress profiles due to an increase of vertical load and its subsequent confining pressure such as:

$$\sigma_V = \sigma_{V0} + \sigma_{Vice} \qquad (2)$$

$$\sigma_H = \frac{\nu}{1-\nu}\sigma_V + T_{cH} \qquad (3)$$

$$\sigma_h = \frac{\nu}{1-\nu}\sigma_V + T_{ch} \qquad (4)$$

in which σ_V, σ_H and σ_h are respectively the vertical, maximum horizontal and minimum horizontal stresses, σ_{V0} is the lithostatic stress, σ_{Vice} the vertical load due to the ice thickness, and T_{cH} and T_{ch} are the major and minor tectonic constant applied horizontally, respectively. σ_{V0} and σ_{Vice} are calculated along depth profiles as a function of the material density and the thickness of each unit. The tectonic constants are calculated as the difference between the measured actual in-situ horizontal stresses and the confining pressure due to the vertical lithostatic load:

$$P_c = \frac{\nu}{1-\nu}\sigma_V \qquad (5)$$

190   We however note that the stresses above a depth of 300 m are not precise (Ask, 2011) probably because too close to

the surface, where the in situ-stresses are estimated to be perturbed. The present day tectonic constant profiles have

been extracted (from Eq. 2-4). They increase linearly with depth and are interpreted to be due to the Atlantic ridge

push (Forsyth and Uyeda, 1975, Grollimund and Zoback, 2000), and are therefore assumed to be constant during the

next glacial cycle.

195   Stress permutations are expected due to strong variations in the stress distribution at depth (Figure 3a). A

hybrid thrust-fault and strike-slip regime is measured in the actual conditions with no ice sheet, with a prominent

proportion of thrust-fault regime above 1 km in the rock mass. An increasing proportion of the strike-slip regime is

calculated with the increasing of ice thickness up to 1.5 km ice sheet. Pure strike-slip regime is expected for ice

thicknesses ranging between 1.5 and 2.2 km and a hybrid strike-slip (at depth) to normal-fault regime (shallow) is

200   expected between 2.2 and 2.5 km of ice. These variations of principal-stress profiles through time and space,

expressed as *ice thickness* $\in [0, 2500]$ m, will be used as a main variable in the parametric study.

The frictional behavior of the fault zones is also a major process to consider as a variable. Measurements of

friction and cohesion values have been done on the Olkiluoto-fault core rocks (Hudson et al., 2008; Mönkkönen et

al., 2013). These estimations give effective macroscopic values of static friction in the range of $\mu \in [0.3, 0.75]$ and

205   cohesion in the range of $C_0 \in [2.7, 4.2]$ MPa. These estimations give a wide range of values that reflects the large

variety of fault rocks observed in dry conditions (breccias, cataclastites, gouges) and for small samples. It is

however worth noting (i) that wetness and fluid pressure can strongly reduce these values, (ii) that it is impossible to

predict in which part of the fault core slip will occur, and (iii) that these measurements (obtained in the tunnel and

from drill cores) are for a very limited part of the entire fault surfaces and do not take into account the integral up-

210   scaled effect. We therefore use static friction and cohesion applied to the entire fault system as variables in a wider

range comparable to the values used for the first models. Static friction and cohesion vary such as $\mu \in [0, 1]$ and C_0

$\in [0, 10]$ MPa, respectively.

In the same way as previously shown, fifty values of each variable, i.e. ice thickness, friction and cohesion

have been chosen, and the fault slip envelope obtained for the Olkiluoto Island fault system separates the parametric

215   domain (here μ, C_0 and ice thickness) in which the faults are unstable (slip) from the domain where the faults are

stable (no slip).

3 Results

3.1 Fault slip envelope

220   The fault slip envelope for a simple elliptical fault (Figure 1) appears mainly sinuous in shape in the direction of θ. Figure 1a shows the model geometric conditions between θ, fault strike, fault dip and the horizontal uniaxial stress applied for this simple-elliptical fault study (also see section 2.1). Note that when θ = 0° or 180°, the angle between the stress axis and the fault surfaces is 60°, the fault dip angle. The 3D geometry of the fault slip envelope (Figure 1b) shows that slip is favored when the uniaxial stress is oblique to fault strike, and the optimal

225   angle slightly changes with the friction coefficient. Consistently with the Mohr-Coulomb theory, fault slip occurs for a wider range of cohesion when friction is low and conversely for a lower range of cohesion when friction is high. Fault slip appears impeded for two main configurations of resolved shear-stress minima; where the uniaxial stress is parallel to the fault surface (θ = 90°) or where it is normal to fault strike (θ = 0° or 180°). This last configuration, which has an angle of 60° between the stress axis and the fault surface, allows fault slip for low friction and impedes

230   slip for high friction.

       For more complex fault geometries, the fault slip envelopes are sinuous in the direction of θ, with symmetric polymodal shapes reflecting the geometry of the fault configurations tested (Figure 2a). The number of modes of fault instability can vary with the friction coefficient, especially in the models containing vertical faults for which variations of θ affect drastically the relative orientation of the uniaxial stress with the fault surface. For the

235   strike-slip configuration, two modes are observed at θ = 0° and 90° for μ = 0 (at 45° of each fault surface) and four modes at θ = 15°, 60°, 105° and 165° close to μ = 0.5 (i.e. uniaxial load at about 30° of each fault surface). The complex synthetic model including the conjugate fault configuration altogether results therefore quite complex in shape but actually does not show strong variations since many fault orientations are represented, and tend to approach the planar shape expected for the case where all the possible fault orientations are represented (see the

240   synthetic case of the sphere, Figure 2b). We also note that fault slip occurs for a wider range of cohesion when friction is low and for a lower range of cohesion when friction is high.

       Similar results can be found for the real fault systems (Figure 3, see references in section 2.1 for the source data). In simple fault geometry such as the Landers or Chimney Rock examples (Figure 3a and b), the common segmentation or conjugate geometries frequently found in fault systems provide quite constant fault orientation

245   through space. This therefore results in significant spatial anisotropy of strength, expressed by a local inflection of

the fault slip envelope as a function of θ (Figure 3d and e). In more complex fault system, such as the Oseberg Syd example (Figure 3c), there are frequently parts of fault surfaces optimally oriented to slip with respect to stress orientation, implying no significant spatial anisotropy of strength (Figure 3f).

In both synthetic and real fault system geometries (Figure 1, 2 and 3), the degree of irregularity of the fault slip envelope appears to be inversely correlated to the degree of orientation anisotropy of the 3D fault system. The fault slip envelopes appear mainly sinuous in shape in the direction of θ, showing the strong influence of the stress orientation on the shape of the fault slip envelope. Fault slip is favored when the uniaxial stress is oblique to fault strike, and the optimal angle slightly changes with the friction coefficient. Conversely, fault slip is impeded for two main configurations of resolved shear-stress minima; where the uniaxial stress is parallel to the fault surface (e.g. see the main deflection at θ ~ 155° on the envelope in Figure 3d) or where it is normal to fault strike (θ ~ 65°). Also note that fault slip occurs for a wider range of cohesion when friction is low and for a lower range of cohesion when friction is high.

The plot of computed displacement distribution along fault is a way to analyse in which place fault is prone to slip with respect to different parametric conditions. Some examples of computed displacement occurring on preferentially oriented parts of the fault surfaces are shown in Figure 4 for the Landers 3D fault geometry. Computed quasi-static fault displacement distribution is shown (blue stars) for end-member conditions of friction, cohesion and stress orientation with respect to the position of the fault slip envelope (note that the colour bar scale of displacement is logarithmic). These plots shows how large values of friction coefficient allow fault to slip, revealing very different amount and distribution of displacement as a function of θ and C_0 (Figure 4b, c and d). Note that for θ = 0° or 90° displacement occurs on complementary places along the faults and with opposite displacement, sinistral and dextral respectively. The effect of mechanical interaction through the stress field (e.g. Willemse et al., 1996), although significantly lower that the role of θ, μ or C_0, is observed at fault segment overlaps. Figure 4d and e show this effect along the displacement pattern of the first fault segment (i.e. the southern segment, see Figure 3a), which is highly asymmetric in places where this segment have the same fault surface orientation, friction and cohesion. Also note that stress magnitude, distribution and orientations can be computed around fault surfaces of each "slipping" model condition. An example of stress perturbation through the stress field is shown in Figure 5 for the condition of θ = 110°, μ = 0.4 and C_0 = 0. Although in the range of possible friction, cohesion and angle of σ_1 with respect to the main fault trend (around 30°), the parametric conditions shown in Figure 5 must be considered as

non-realistic since the stress loading is purely uniaxial. The absence of stress perturbation in orientation is due to this uniaxial condition and the absence of fluid pressure in this parametric study (see Kattenhorn et al., 2000 and Maerten et al, 2018). More realistic stress conditions must consider the 3D tensor and its variation through space and time.

3.2 The Olkiluoto fault system

The 3D shape of the fault slip envelope obtained using stress variations as proposed in section 2.2 is quite simple in its geometry, with a curvature in the upper corner where cohesion and ice thickness are low, and friction is relatively high (Figure 6c). This reveals that fault slip is promoted for small ice thicknesses (or vertical load) in thrust-fault regime, especially for low cohesion, allowing slip even for relatively high friction values. Other envelopes (pink) are shown in the slip domain of the diagram. These surfaces are not fault slip envelopes, but envelopes of values of equal maximum quasi-static displacement computed along faults, calculated in each model. These envelopes, which depict 2 specific values of computed maximum displacement for different mechanical and loading conditions, mimic the shape of the fault slip envelope in the slip domain. They confirm the shape of the slip envelope and reveal that the largest ability of fault to accumulate displacement is expected for models with unrealistic conditions of no fault friction, no cohesion and no ice sheet. Since quasi-static displacement takes into account fault interaction through the stress field, and that fault slip envelope does not, the similar shape of these three envelopes reveals the lesser influence of fault mechanical interaction compare to the effect of varying friction, cohesion and stresses in the ranges considered in this study.

Quasi-static displacement distributions along fault slipping patches are shown in Figure 7 in colored areas (the colour bar scale is logarithmic) containing streamlines representing the orientation of fault slip, referred to as "slickenlines". Displacements are computed for individual models of parametric conditions shown on the envelope with blue stars. We chose to show end member cases, i.e. far and progressively closer to the main fault slip envelope, with roughly different parametric conditions. Displacement distribution varies from one model to another and is heterogeneous within a same model as a function of fault plane orientation, friction and applied stress state with changing ice thickness. Consistently with the shape of the envelopes, the ability of slip to initiate and accumulate is enhanced for conditions of low friction, cohesion and no ice sheet cover, for which most of the faults are slipping (maximum displacement lower than 0.7 m). Closer to the main fault slip envelope, slip occurs on areas

11

restricted to the lower or upper parts of the faults, better oriented to slip (upper part) and/or for which the differential stress applied in remote condition is the largest (lower part). Fault slip close to the Earth's surface is possible only for conditions of no ice sheet cover and moderate friction (0.15 to 0.3). Slickenlines of reverse and strike-slip

305   movements can slightly change along a single fault surface. These changes in orientation are mainly governed by changing remote stress state with depth (Figure 6a).

4 Discussion

We defined fault slip envelope and therefore quantified the strength of large rock volume containing faults

310   as a function of friction, cohesion and remote stresses. In the first order, our parametric study of simple to complex fault system reveals that their strength can be assessed as a function of their degree of geometric complexity. The more complex is the geometry, the simpler are the fault slip envelopes. Complex fault systems always have optimally oriented fault surfaces that can slip with respect to the boundary stress conditions applied. In contrast, fault systems having limited fault orientations relative to the principal remote stresses, provide strong strength

315   anisotropy such as revealed by strong curvature of the fault slip envelope in the direction of θ. Also worth noting is that the strength anisotropy varies with the values of friction of the fault surfaces. This general behaviour is inherent to the Mohr-Coulomb frictional-slip theory, for which fault slip with respect to the stress orientation and state depends on the friction coefficient (Hatheway and Kiersch, 1989; Scholz, 2019).

The case study of the Olkiluoto nuclear waste repository site allowed us to apply this technique on a fault

320   system subjected to realistic stress loading conditions. The resulting fault slip envelope for the Olkiluoto system show the importance of the 3D geometry of the fault system, but also the critical importance of the applied geological stresses. For the present day context of no ice sheet (interglacial period), this fault system is subjected to a thrust-fault stress regime governed by the E-W push from the mid-Atlantic ridge. This geological context seems to provide the best conditions for fault slip because of the highest resolved shear stress on low dipping fault surfaces.

325   Such fault surfaces are optimally oriented to slip under a thrust-fault stress regime with S_1 oriented E-W and with large values of differential stress applied, especially close to the Earth's surface for these conditions of no ice thickness (Fig. 6a, 0 m of ice). Even for high friction values, optimally-oriented fault surfaces could therefore be critically stressed in the present day.

Although the actual conditions provide the largest resolved shear stress on fault plane, the main results obtained are in agreement with the actual conditions observed at the Olkiluoto repository site, where no slip is monitored or observed along faults under the actual conditions. Although probably variable along fault surfaces, the fault rock mechanical properties derived from mechanical tests suggest a static friction and cohesion larger than the conditions computed to allow fault slip. The worst case scenario would corresponds to the upper right 3D model result shown in Figure 7 ($\mu = 0.3$, $C_0 = 4$ Mpa, no ice thickness) where fault slip might occur in a very limited upper part of the fault model. Also note that the actual stress profiles (referred to as "no ice thickness", Figure 6a, 0 m of ice) are not well defined close to the earth's surface and probably overestimated because of the loss of rock cohesion due to the presence of open fracture patterns and rock alteration (Ask, 2011; Hudson et al., 2008; Mönkkönen et al., 2013).

The increase of thickness of an ice sheet implies progressive stress permutation to the strike-slip regime in the stress profiles (Figure 6a). The general low dip of the faults (non-optimal orientation) combined with a low differential stress, inherent to this strike-slip regime, provide conditions for low resolved shear stresses on faults, and therefore better general strength of the fault system (also see Johnston, 1987). The planar and vertical shape of the fault slip envelope in this lower part of the diagram reveals the little dependence of fault strength on the vertical load increase, here value of S_2 (or the Lode angle). Given the range of friction and cohesion estimated using mechanical tests, such conditions of increasing ice thickness must be unfavorable for fault slip. However, as mentioned in section 2.2, such range might strongly evolve through time and space, outside of the sampled areas, due to the presence of fluids or variations of fault rocks properties.

A potential limitation of the proposed technique relies on the uncertainty and biases of the 3D fault surface discretization. In the example of Olkiluoto, uncertainties of fault surface geometry were estimated from a significant amount of data available from bore hole, seismic profiles, tunnel wall observations and outcrop measurements (Mattila et al., 2007). Truncation bias is here defined by not considering the faults smaller than 100 m length estimated to allow incremental displacement lower than 10^{-2} m (Wells and Copersmith, 1994). Variability or uncertainty of in-situ stresses and rock material properties estimated from bore hole and rock tests are not considered as limitations since they are used to constrain their range of variability in the parametric study (see section 2.2). This approach is actually particularly suitable to address uncertainties in input data and any hazard assessment. On the other hand, oversight or mistakes in the choice of the variable considered in the model can be a major limitation in

the approach. In the Olkiluoto example we chose to consider friction, cohesion and especially the stress state as the main variables, rather than for example the role of water pressure. Although variation in hydraulic head in the vadose/aquifer zone considered is expected during the glacial period (Lemieux et al., 2008), it has no effect on

360   anisotropy of strength since water pressure is isotropic, and thus doesn't change the shape of the fault slip envelope. Furthermore, expected water pressures are one order of magnitude lower (several MPa) than tectonic stresses (20 to 60 MPa), and would very slightly displace the fault slip envelope toward the right hand of the diagram shown in Figure 6c and 7. The effect of water on static friction weakening of the altered fault rocks is probably much more important (more than 50% reduction of friction in clays, Morrow et al., 2000), and is indirectly considered in the

365   range of friction used in the parametric study ($\mu \in [0, 1]$). A last limitation concerns the quasi-static elastic fault displacement patterns computed in places where slip occurs (Figure 5). As mentioned in the method section, this displacement distribution must be seen as fault ability to initiate and accumulate slip. Even though quasi-static models generally provide good results (e.g. Pollard and Fletcher, 2005; p308, chapter 8.3.3 and Figure 8.15), realistic co-seismic displacement distribution and subsequent stress perturbation in the surrounding can be better

370   approached using dynamic rupture propagation processes and dynamic friction laws in softening or hardening fault rocks as a function of material properties and new stress field around the first slipping fault in the model.

5 Conclusion

375   A new tool referred to as "fault slip envelope" is proposed in order to provide complementary analysis to the conventional methods used for fault slip or slip tendency, such as:

(1) Fault slip is calculated along simple or very complex fault geometry on DFN using the resolved shear and normal stresses with respect to the Mohr Coulomb's frictional slip theory and quasi-static elastic behavior. This method allows considering friction and cohesion as potential variables through space and time.

380   (2) Combining 3D boundary element model and fast computation method allows to run thousands of forward simulations in very short time, and therefore to provide full parametric study with a wide range of variable mechanical conditions such as stress orientation and magnitude.

(3) This technique allows for the first time to propose "fault slip envelopes" which quantify fault system strength magnitude and anisotropy as a function of important parameters, which are either unknown and/or

14

385   considered as variable through time and space. This can be useful to address uncertainties in input data for hazard assessment.

(4) We also calculate fault displacement based on quasi-static elastic solution allowing mechanical interaction through the stress field, in places where the Coulomb's criterion is reached along each fault of a DFN.

390   The quantification of the strength of fault systems in 3D underlines the importance of accuracy in deterministic studies of geological structures and stresses. Beyond its societal application to fault slip hazard, geological storage, geothermal systems, and reservoirs leaks, this technology also provides new considerations and perspectives in the analysis of fault systems and Earth's crust strength. Major earthquakes at plate boundaries occur on relatively simple fault systems, such as large strike-slips faults or subduction plate megathrusts (Berryman et al.,

395   2012; Chester et al., 2013; also see Figure 3a), where the strength is definitely anisotropic and thoroughly depends on stress orientation and fault zone properties (e.g. Figure 3d). It is nevertheless also well known that large earthquakes can occur on more complex fault geometries, as for example in the Kaikoura and Darfield fault systems in New Zaeland's south island (Beavan et al., 2012; Hamling et al., 2017; Ulrich et al., 2019) or in the Sierra Madre–Cucamonga thrust fault system in southern California (Anderson et al., 2003). In such a case, fault system

400   strength is probably more isotropic, and fault slip depends more on static friction along faults than on stress orientation (e.g. Figure 3f). This difference in domain of stability, allows quantifying the bulk strength of the brittle crust, which results lower for complex fault geometry rather than simple one for equivalent frictional and remote stress condition, as recently observed in experimental modeling of complex versus simple subduction interface (Van Rijsingen et al., 2019). As much as frictional properties or pore-pressure, the degree of complexity of a fault system

405   constitute the basic premises for easier crustal stress relaxation and prevention of major slip events. Consequently, the precise definition and quantification of the strength in the brittle crust relies on the precise knowledge of 3D fault geometry, constitution and stresses on each study site. Significant progress in this field imposes a challenge for future geosciences.

410   **Acknowledgments**

415

References

Aaltonen, I., Lahti, M., Engström, J., Mattila, J., Paananen, M., Paulamäki, S., Gehör, S, Kärki, A., Ahokas, T., Torvela, T., and Front, K.: Geological Model of the Olkiluoto Site version 2, Posiva Working Report 70, available at: http://www.posiva.fi/files/1439/WR_2010-70_web.pdf, 2010.

420   Alvarez del Castillo, A., Alaniz-Alvarez, A. A., Nieto-Samaniego, A. F., Xu, S., Ochoa-Gonzales, G. H., and Velasquillo-Martinez, L. G.: Software for determining the direction of movement, shear and normal stresses of a fault under a determined stress state, Computer and Geosciences, 104, 84-92, http://dx.doi.org/10.1016/j.cageo.2017.03.006, 2017

Anderson, G., Aagaard, B., and Hudnut, K.: Fault Interactions and Large Complex Earthquakes in the Los Angeles
425   Area, Science 302, 1946, DOI: 10.1126/science.1090747, 2003.

Arvidsson, R.: Fennoscandian earthquakes: Whole crust rupturing related to postglacial rebound: Science 274, 744-746, 1996.

Arthaud, F.: Méthode de détermination graphique des directions de raccourcissement, d'allongement et intermédiaire d'une population de failles, B Soc Geol Fr, 7 (XI), 729–737, 1969.

430   Ask, D.: Semi-Integration of Overcoring Stress Data and Review of Rock Stress Data at the Olkiluoto Site, Posiva Working Report 16, available at: http://www.posiva.fi/files/1705/WR_2011-16web.pdf, 2011.

Beavan, J., Motagh, M., Fielding, E. J., Donnelly, N. and Collett, D.: Fault slip models of the 2010–2011 Canterbury, New Zealand, earthquakes from geodetic data and observations of postseismic ground deformation, N. Z. J. Geol. Geophys., 55(3), 207–221, doi:10.1080/00288306.2012.697472, 2012.

435   Berryman, K. R., Cochran, U. A., Clark, K. J., Biasi, G. P., Langridge, R. M., and Villamor, P.: Major Earthquakes Occur Regularly on an Isolated Plate Boundary Fault, Science 336, 1690-1693, DOI: 10.1126/science.1218959, 2012.

Berger, A., and Loutre, M.F. : Paleoclimate sensitivity to CO2 and insolation. Ambio 26, 32-37, 1997

Brantut, N., Heap, M. J., Meredith, P. G. and Baud, P.: Time-dependent cracking and brittle creep in crustal rocks: A

440   review, Journal of Structural Geology, 52, 17–43, doi:10.1016/j.jsg.2013.03.007, 2013.

Byerlee, J. D.: Friction of rocks, Pure Appl Geophys, 116, 615-626, 1978.

Chester, F. M., Rowe, C., Ujiie, K., Kirkpatrick, J., Regalla, C., Remitti, F., Moore, J. C., Toy, V., Wolfson-

Schwehr, M., Bose, S., Kameda, J., Mori, J. J., Brodsky, E. E., Eguchi, N. and Toczko, S.: Structure and

Composition of the Plate-Boundary Slip Zone for the 2011 Tohoku-Oki Earthquake, Science, 342(6163),

445   1208, doi:10.1126/science.1243719, 2013.

Collettini, C., Niemeijer, A., Viti, C. and Marone, C.: Fault zone fabric and fault weakness, Nature, 462, 907, 2009.

Collettini, C., and Trippetta, F.: A slip tendency analysis to test mechanical and structural control on aftershock

rupture planes, Earth and Planetary Science Letters, 255, 402–413, 2007.

Crider, J. G. and Pollard, D. D.: Fault linkage: Three-dimensional mechanical interaction between echelon normal

450   faults, Journal of Geophysical Research: Solid Earth, 103(B10), 24373–24391, doi:10.1029/98JB01353,

1998.

Faulkner, D. R., Mitchell, T. M., Healy, D. and Heap, M. J.: Slip on "weak" faults by the rotation of regional stress

in the fracture damage zone, Nature, 444, 922, 2006.

Forsyth, D. and Uyedaf†, S.: On the Relative Importance of the Driving Forces of Plate Motion, Geophysical

455   Journal of the Royal Astronomical Society, 43(1), 163–200, doi:10.1111/j.1365-246X.1975.tb00631.x, 1975.

Hackston, A. and Rutter, E.: The Mohr–Coulomb criterion for intact rock strength and friction – a re-evaluation and

consideration of failure under polyaxial stresses, Solid Earth, 7(2), 493–508, doi:10.5194/se-7-493-2016,

2016.

Hakkala, M., Siren, T., Kemppainen, K., Christiansson, R., and Martin, D.: In Situ Stress Measurement with the

460   New LVDT-cell – Method Description and Verification, Posiva Working Report 2012-43, available at:

http://www.posiva.fi/files/3448/POSIVA_2012-43.1.pdf, 2013.

Hamling, I. J., Hreinsdóttir, S., Clark, K., Elliott, J., Liang, C., Fielding, E., Litchfield, N., Villamor, P., Wallace, L.,

Wright, T. J., D'Anastasio, E., Bannister, S., Burbidge, D., Denys, P., Gentle, P., Howarth, J., Mueller, C.,

Palmer, N., Pearson, C., Power, W., Barnes, P., Barrell, D. J. A., Van Dissen, R., Langridge, R., Little, T.,

465   Nicol, A., Pettinga, J., Rowland, J. and Stirling, M.: Complex multifault rupture during the 2016 M w 7.8

Kaikōura earthquake, New Zealand, Science, 356(6334), eaam7194, doi:10.1126/science.aam7194, 2017.

Hatheway, A. W., and Kiersch, G. A. (Eds): Engineering properties of rock, R.S. Carmichael, Practical Handbook of

Physical Properties of Rocks and Minerals, CRC Press, Boca Raton, 672-715, 1989.

Healy, D., Blenkinsop, T. G., Timms, N. E., Meredith, P. G., Mitchell, T. M. and Cooke, M. L.: Polymodal faulting:

470   Time for a new angle on shear failure, Journal of Structural Geology, 80, 57–71,

doi:10.1016/j.jsg.2015.08.013, 2015.

Holdsworth, R. E.: Weak Faults--Rotten Cores, Science, 303(5655), 181, doi:10.1126/science.1092491, 2004.

Hudson, J. A., Cosgrove, J. W., and Johansson, E.: Estimating the Mechanical Properties of the Brittle Deformation

Zones at Olkiluoto, Posiva Working Report 67, available at: http://www.posiva.fi/files/800/WR2008-

475   67web.pdf, 2008.

Jaeger J. C. and Cook N. G. W. (Eds): Fundamentals of Rock Mechanics, Chapman and Hall, New York, 1979.

Johnston, A. C.: Suppression of earthquakes by large continental ice sheets, Nature, 330(6147), 467–469,

doi:10.1038/330467a0, 1987.

Karlstrom, K. E. and Williams, M. L.: Heterogeneity of the middle crust: Implications for strength of continental

480   lithosphere, Geology, 26(9), 815–818, doi:10.1130/0091-7613(1998)026<0815:HOTMCI>2.3.CO;2, 1998.

Kattenhorn, S. A., Aydin, A. and Pollard, D. D.: Joints at high angles to normal fault strike: an explanation using 3-

D numerical models of fault-perturbed stress ®elds p, J. Struct. Geol., 23, 2000.

Kattenhorn, S. A., Pollard, D. D.: Integrating 3D seismic data, field analogs and mechanical models in the analysis

of segmented normal faults in the Wytch Farm oil field, southern England, AAPG Bull, 85, 1183–1210,

485   2001.

Kuivamäki, A., Vuorela, P., and Paananen, M.: Indications of Postglacial and Recent Bedrock Movements in

Finland and Russian Karelia, Geological Survey of Finland Report, YST-99, 1998.

Lejri, M., Maerten, F., Maerten, L. and Soliva, R.: Accuracy evaluation of both Wallace-Bott and BEM-based

paleostress inversion methods, Tectonophysics, 694, 130–145, doi:10.1016/j.tecto.2016.11.039, 2017.

490   Lemieux, J.-M., Sudicky, E. A., Peltier, W. R. and Tarasov, L.: Dynamics of groundwater recharge and seepage

over the Canadian landscape during the Wisconsinian glaciation, Journal of Geophysical Research: Earth

Surface, 113(F1), doi:10.1029/2007JF000838, 2008.

Lisle, R. J. and Srivastava, D. C.: Test of the frictional reactivation theory for faults and validity of fault-slip analysis, Geology, 32(7), 569–572, doi:10.1130/G20408.1, 2004.

495   Lovely, P. J., Pollard, D. D., and Mutlu, O.: Regions of Reduced Static Stress Drop near Fault Tips for Large Strike-Slip EarthquakesRegions of Reduced Static Stress Drop near Fault Tips for Large Strike-Slip Earthquakes, Bulletin of the Seismological Society of America, 99(3), 1691–1704, doi:10.1785/0120080358, 2009.

Madden, E. H., Maerten, F. and Pollard, D. D.: Mechanics of nonplanar faults at extensional steps with application to the 1992 M 7.3 Landers, California, earthquake: J. Geophys. Res. Solid Earth, 118(6), 3249–3263,

500   doi:10.1002/jgrb.50237, 2013.

Maerten, F., Maerten, L. and Cooke, M.: Solving 3D boundary element problems using constrained iterative approach, Computational Geosciences, 14(4), 551–564, doi:10.1007/s10596-009-9170-x, 2010.

Maerten, L., Maerten, F. and Lejri, M.: Along fault friction and fluid pressure effects on the spatial distribution of fault-related fractures, J. Struct. Geol., 108, 198–212, doi:10.1016/j.jsg.2017.10.008, 2018.

505   Maerten, F., Maerten, L. and Pollard, D. D.: iBem3D, a three-dimensional iterative boundary element method using angular dislocations for modeling geologic structures, Computers & Geosciences, 72, 1–17, doi:10.1016/j.cageo.2014.06.007, 2014.

Maerten, L., Pollard, D. D. and Maerten, F.: Digital mapping of three-dimensional structures of the Chimney Rock fault system, central Utah, Journal of Structural Geology, 23(4), 585–592, doi:10.1016/S0191-

510   8141(00)00142-5, 2001.

Maerten, L., Gillespie, P. and Pollard, D. D.: Effects of local stress perturbation on secondary fault development, Journal of Structural Geology, 24(1), 145–153, doi:10.1016/S0191-8141(01)00054-2, 2002.

Marrett, R. and Allmendinger, R. W.: Kinematic analysis of fault-slip data, Journal of Structural Geology, 12(8), 973–986, doi:10.1016/0191-8141(90)90093-E, 1990.

515   Mattila, J. and Viola, G.: New constraints on 1.7 Gyr of brittle tectonic evolution in southwestern Finland derived from a structural study at the site of a potential nuclear waste repository (Olkiluoto Island), Journal of Structural Geology, 67, 50–74, doi:10.1016/j.jsg.2014.07.003, 2014.

McLaskey, G. C., Thomas, A. M., Glaser, S. D. and Nadeau, R. M.: Fault healing promotes high-frequency earthquakes in laboratory experiments and on natural faults, Nature, 491, 101, 2012.

520   Mönkkönen, H., Hakkala, M., Paananen, M., and Laine, E. : Onkalo Rock Mechanics Model Version 2, Posiva

Working Report 07, available at http://www.posiva.fi/files/2026/WR_2012-07web.pdf, 2012.

Moeck, I., Kwiatek, G. and Zimmermann, G.: Slip tendency analysis, fault reactivation potential and induced seismicity in a deep geothermal reservoir, Journal of Structural Geology, 31(10), 1174–1182, doi:10.1016/j.jsg.2009.06.012, 2009.

525   Morris, A., Henderson, D. B. and Ferrill, D. A.: Slip-tendency analysis and fault reactivation, Geology, 24(3), 275–278, doi:10.1130/0091-7613(1996)024<0275:STAAFR>2.3.CO;2, 1996.

Morrow, C. A., Moore, D. E. and Lockner, D. A.: The effect of mineral bond strength and adsorbed water on fault gouge frictional strength, Geophysical Research Letters, 27(6), 815–818, doi:10.1029/1999GL008401, 2000.

Neves, M. C., Paiva, L. T. and Luis, J.: Software for slip-tendency analysis in 3D: A plug-in for Coulomb,

530   Computers & Geosciences, 35(12), 2345–2352, doi:10.1016/j.cageo.2009.03.008, 2009.

Nicol, A., Watterson, J., Walsh, J. J. and Childs, C.: The shapes, major axis orientations and displacement patterns of fault surfaces, Journal of Structural Geology, 18(2), 235–248, doi:10.1016/S0191-8141(96)80047-2, 1996.

Pollard, D. D. and Fletcher, R. C. (Eds): Fundamentals of Structural Geology, Cambridge University Press, 2005.

Reyners, M., Eberhart-Phillips, D. and Martin, S.: Prolonged Canterbury earthquake sequence linked to widespread

535   weakening of strong crust, Nature Geoscience, 7, 34, 2013.

Rutter, E. H. and Glover, C. T.: The deformation of porous sandstones; are Byerlee friction and the critical state line equivalent?, Journal of Structural Geology, 44, 129–140, doi:10.1016/j.jsg.2012.08.014, 2012.

Scholz, C. H.: The Mechanics of Earthquakes and Faulting, 3rd ed., Cambridge University Press, Cambridge., 2019.

Sjöberg, J.: Overcoring Rock Stress Measurements in Borehole OL-KR24, Olkiluoto, Posiva Working Report 60,

540   available at http://www.posiva.fi/files/2238/POSIVA-2003-60_Working-report_web.pdf, 2003.

Skinner, B. J., and Porter, S. C., (Eds): Physical Geology, John Wiley & Sons, 1987.

Soliva, R., Benedicto, A., Schultz, R. A., Maerten, L. and Micarelli, L.: Displacement and interaction of normal fault segments branched at depth: Implications for fault growth and potential earthquake rupture size, Journal of Structural Geology, 30(10), 1288–1299, doi:10.1016/j.jsg.2008.07.005, 2008.

545   Thomas, A. L.: Poly3D: a three-dimensional, polygonal element, displacement discontinuity boundary element computer program with applications to fractures, faults, and cavities in the earth's crust, M.S. thesis, Stanford University, Stanford, California, USA, 1993.

Townend, J. and Zoback, M. D.: How faulting keeps the crust strong, Geology, 28(5), 399–402, doi:10.1130/0091-

7613(2000)28<399:HFKTCS>2.0.CO;2, 2000.

550 Ulrich, T., Gabriel, A.-A., Ampuero, J.-P. and Xu, W.: Dynamic viability of the 2016 Mw 7.8 Kaikōura earthquake cascade on weak crustal faults, Nat. Commun., 10(1), doi:10.1038/s41467-019-09125-w, 2019.

Van Rijsingen, E., Funiciello, F., Corbi, F. and Lallemand, S.: Rough Subducting Seafloor Reduces Interseismic Coupling and Mega-Earthquake Occurrence: Insights From Analogue Models, Geophysical Research Letters, 0(0), doi:10.1029/2018GL081272, 2019.

555 Wells, D. L. and Coppersmith, K. J.: New empirical relationships among magnitude, rupture length, rupture width, rupture area, and surface displacement, Bulletin of the Seismological Society of America, 84(4), 974–1002, 1994.

Wibberley, C. A. J., Yielding, G. and Di Toro, G.: Recent advances in the understanding of fault zone internal structure: a review, Geological Society, London, Special Publications, 299(1), 5, doi:10.1144/SP299.2, 2008.

560 Willemse, E. J. M., Pollard, D. D. and Aydin, A.: Three-dimensional analyses of slip distributions on normal fault arrays with consequences for fault scaling, J. Struct. Geol., 18(2–3), 295–309, doi:10.1016/S0191-8141(96)80051-4, 1996.

Yukutake, Y., Takeda, T. and Yoshida, A.: The applicability of frictional reactivation theory to active faults in Japan based on slip tendency analysis, Earth and Planetary Science Letters, 411, 188–198,

565 doi:10.1016/j.epsl.2014.12.005, 2015.

570

575

580

585

Figure Captions

590   **Figure 1 (2 column fitting image). Fault slip envelope of a simple-planar elliptical fault of 60° dip. (a) Scheme of the relationship between fault strike, dip and remote uniaxial stress orientation. (b) Fault slip envelope expressed as static friction (μ), cohesion (C_0) and uniaxial stress angle (θ). The stable (No slip) and unstable (Slip) graphical domains are shown on either side of the fault slip envelope.**

595   **Figure 2 (*2 column fitting image*). Synthetic 3D fault geometries and their fault slip envelopes. (a) Variable 3D intersecting fault geometries and related fault slip envelope calculated with the same variables than Figure 1. (b) Theoretical case of a sphere and its fault slip envelope calculated with the same variables than (a) and Figure 1. The small empty box indicates the parameters on each axis of the envelope diagrams shown in (a) and (b).**

600   **Figure 3 *(2 column fitting image)*. Examples of 3D fault system geometry, from a simple to a very complex case, and related fault slip envelopes. (a) The Landers strike-slip fault segments. (b) The Chimney rock conjugate strike-slip fault system. (c) The Oseberg Syd normal fault system. (d), (e) and (f) are fault slip envelopes for each fault system, defining fault system stability for variable uniaxial stress orientation (θ), static friction (μ) and cohesion (C_0) on fault surfaces. Colours in (a, b and c) correspond to different fault surfaces and allow an individual fault to be identified.**

605

22

Figure 4 *(2 column fitting image)*. **Examples of 3D quasi-static fault displacement distribution on the Landers model for different mechanical conditions and uniaxial stress orientation. (a) Fault slip envelope shown in Figure 3d with reported specific model conditions used for figure parts b, c, d and e (bleu stars). (b) Displacement distribution for $\mu = 1$, $C_0 = 0$ MPa and $\theta = 0°$. (c) Displacement distribution for $\mu = 1$, $C_0 = 3$ MPa and $\theta = 0°$. (d) Displacement distribution for $\mu = 1$, $C_0 = 0$ MPa and $\theta = 90°$. (e) Displacement distribution for $\mu = 0$, $C_0 = 0$ MPa and $\theta = 180°$. The colour bar scale for displacement is logarithmic.**

Figure 5 *(2 column fitting image)*. **Examples of quasi-static stress distribution of σ_1 (a) and Maximum Coulomb's shear stress (b) around the Landers fault model, computed for $\theta = 110°$, $\mu = 0.4$ and $C_0 = 0$.**

Figure 6 *(2 column fitting image)*. **Case study of the Olkiluoto fault system. (a) Stress state in the rock mass applied to the fault system, measured at the present day (0 m of ice) and calculated for future conditions as a function of the thickness of an ice sheet cover (for 1500 m and 2500 m of ice). The maximum horizontal stress (σ_H) is oriented E-W. (b) 3D geometry of the fault system at the nuclear site. (c) Fault slip envelope of the Olkiluoto fault system (red surface), calculated using variable friction, cohesion and stress profiles derived from 0 to 2500 m of ice sheet cover (a). The two pink surfaces are envelopes of values of equal maximum quasi-static displacement computed along faults, each one corresponding to a specific value of displacement (0.02 m and 0.06 m). See the main text for further details.**

Figure 7 *(2 column fitting image)*. **Examples of 3D quasi-static fault displacement distribution on the Olkiluoto model for different loading and fault properties conditions indicated on the fault slip diagram by blue stars. Stream lines on fault surfaces are slickenlines. The colour bar scale for displacement is logarithmic.**
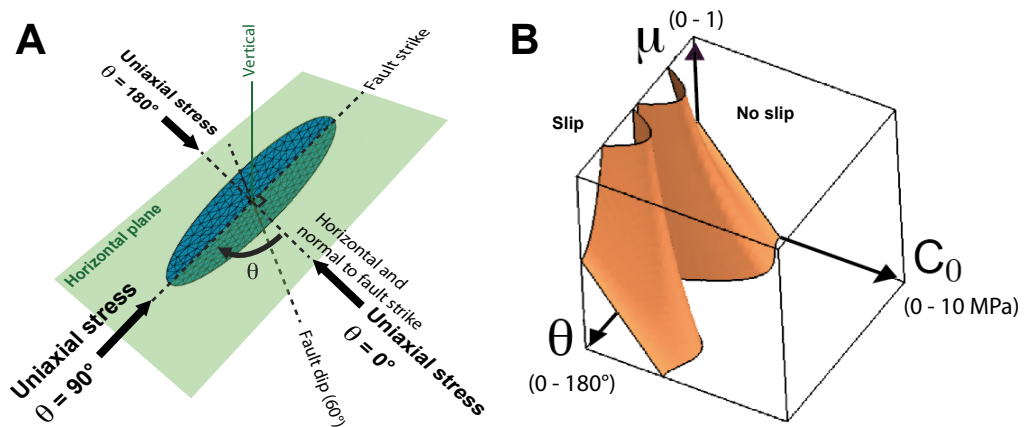
Figure 1

Figure 1 (2 column fitting image). Fault slip envelope of a simple-planar elliptical fault of 60° dip. (a) Scheme of the relationship between fault strike, dip and remote uniaxial stress orientation. (b) Fault slip envelope expressed as static friction (μ), cohesion (C0) and uniaxial stress angle (θ). The stable (No slip) and unstable (Slip) graphical domains are shown on either side of the fault slip envelope.
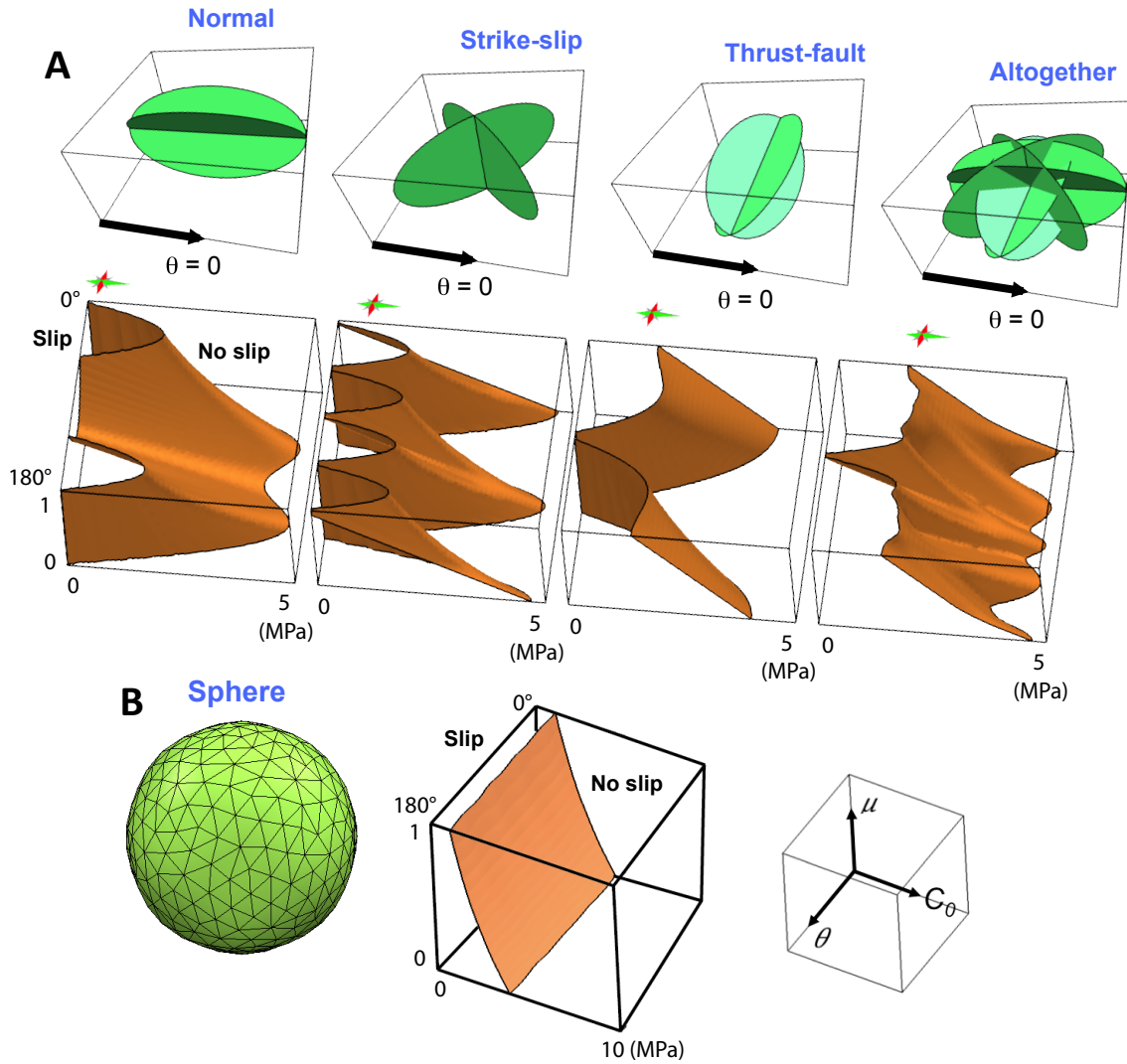
Figure 2

Figure 2 (2 column fitting image). Synthetic 3D fault geometries and their fault slip envelopes. (a) Variable 3D intersecting fault geometries and related fault slip envelope calculated with the same variables than Figure 1. (b) Theoretical case of a sphere and its fault slip envelope calculated with the same variables than (a) and Figure 1. The small empty box indicates the parameters on each axis of the envelope diagrams shown in (a) and (b).
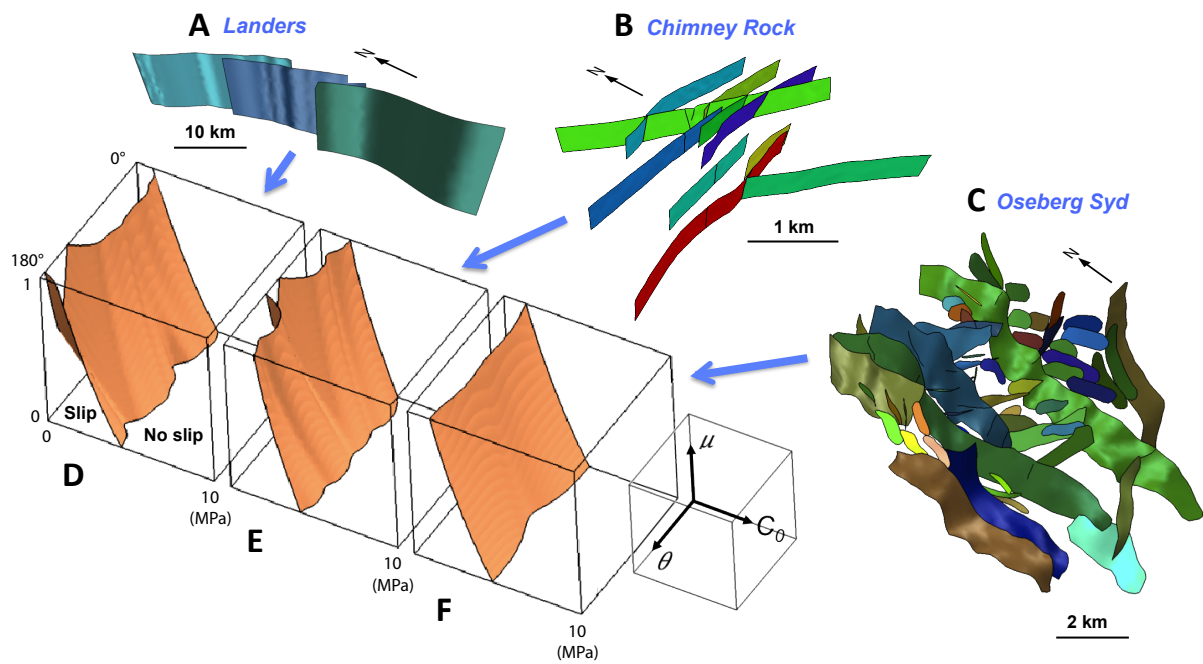
Figure 3

A *Landers*

B *Chimney Rock*

C *Oseberg Syd*

10 km

1 km

2 km

0°

180°
1

Slip

No slip

0
0

D

10
(MPa)

E

10
(MPa)

F

10
(MPa)

μ

C₀

θ

Figure 3 (2 column fitting image). Examples of 3D fault system geometry, from a simple to a very complex case, and related fault slip envelopes. (a) The Landers strike-slip fault segments. (b) The Chimney rock conjugate strike-slip fault system. (c) The Oseberg Syd normal fault system. (d), (e) and (f) are fault slip envelopes for each fault system, defining fault system stability for variable uniaxial stress orientation (θ), static friction (µ) and cohesion (C0) on fault surfaces. Colours in (a, b and c) correspond to different fault surfaces and allow an individual fault to be identified.
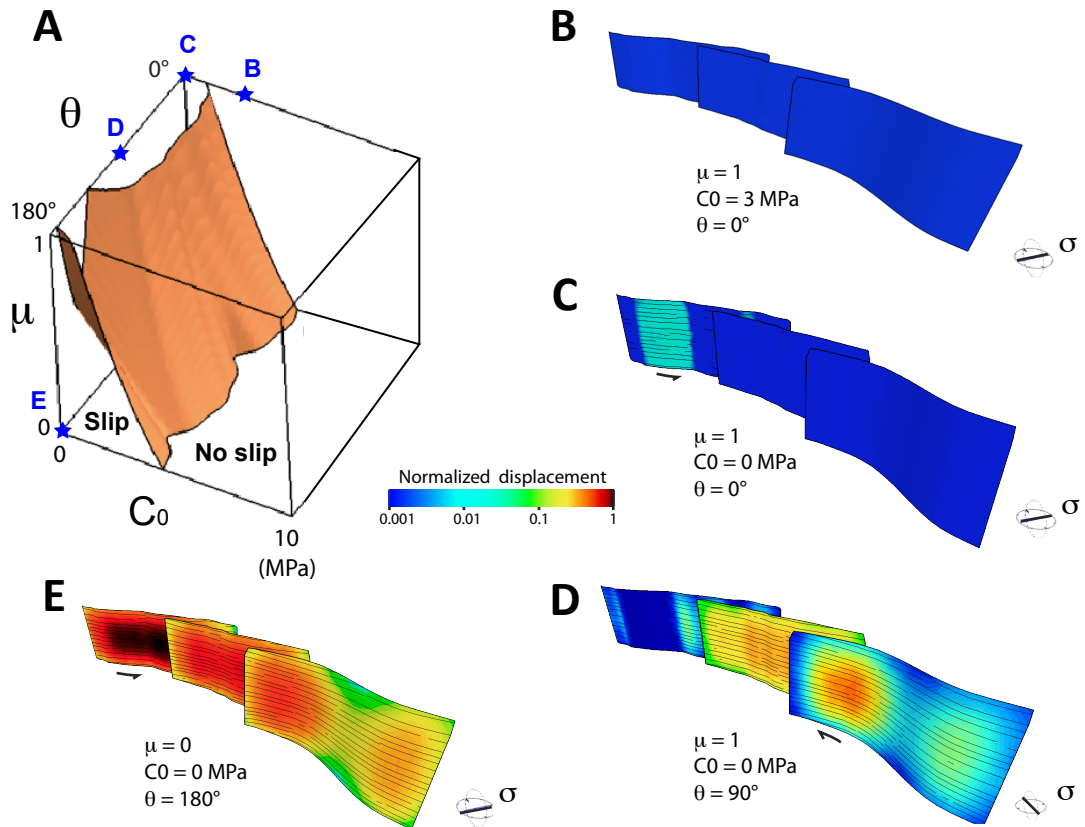
Figure 4

Figure 4 (2 column fitting image). Examples of 3D quasi-static fault displacement distribution on the Landers model for different mechanical conditions and uniaxial stress orientation. (a) Fault slip envelope shown in Figure 3d with reported specific model conditions used for figure parts b, c, d and e (bleu stars). (b) Displacement distribution for μ = 1, C0 = 0 MPa and θ = 0°. (c) Displacement distribution for μ = 1, C0 = 3 MPa and θ = 0°. (d) Displacement distribution for μ = 1, C0 = 0 MPa and θ = 90°. (e) Displacement distribution for μ = 0, C0 = 0 MPa and θ = 180°. The colour bar scale for displacement is logarithmic.

Figure 5

A Maximum principal stress σ1   **B** Maximum Coulomb's shear stress

1

Normalized
displacement
on fault and stresses
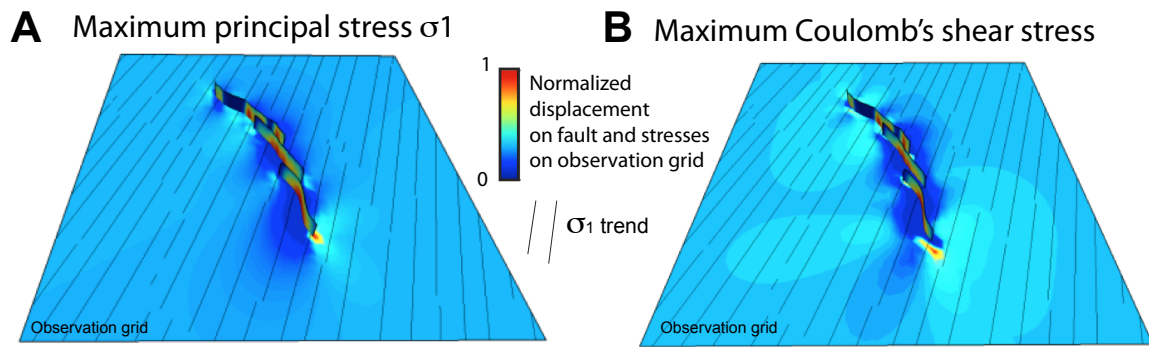on observation grid

0

σ1 trend

Observation grid

Figure 5 (2 column fitting image). Examples of quasi-static stress distribution of σ1 (a) and Maximum Coulomb's shear stress (b) around the Landers fault model, computed for θ = 110°, μ = 0.4 and C0 = 0.
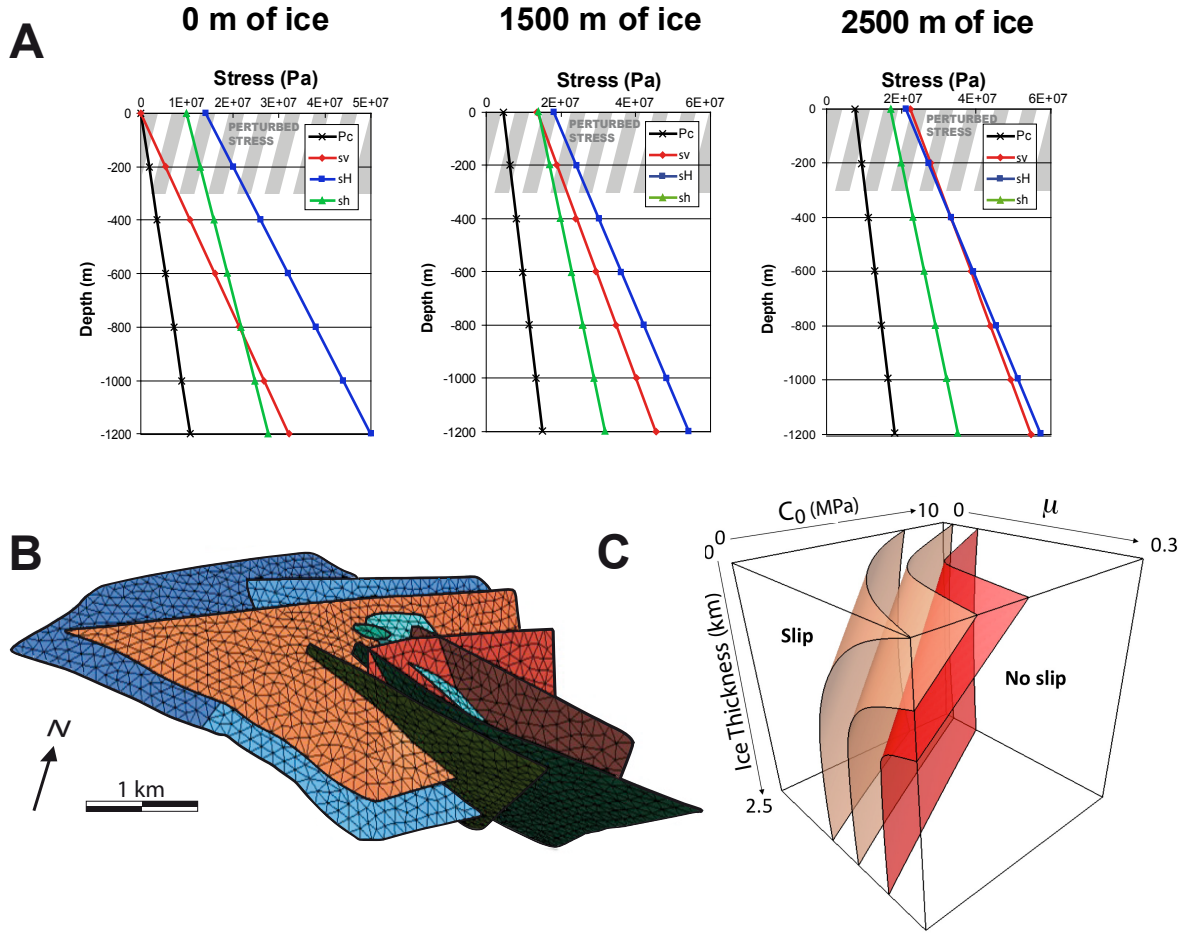
Figure 6

Figure 6 (2 column fitting image). Case study of the Olkiluoto fault system. (a) Stress state in the rock mass applied to the fault system, measured at the present day (0 m of ice) and calculated for future conditions as a function of the thickness of an ice sheet cover (for 1500 m and 2500 m of ice). The maximum horizontal stress (σH) is oriented E-W. (b) 3D geometry of the fault system at the nuclear site. (c) Fault slip envelope of the Olkiluoto fault system (red surface), calculated using variable friction, cohesion and stress profiles derived from 0 to 2500 m of ice sheet cover (a). The two pink surfaces are envelopes of values of equal maximum quasi-static displacement computed along faults, each one corresponding to a specific value of displacement (0.02 m and 0.06 m). See the main text for further details.
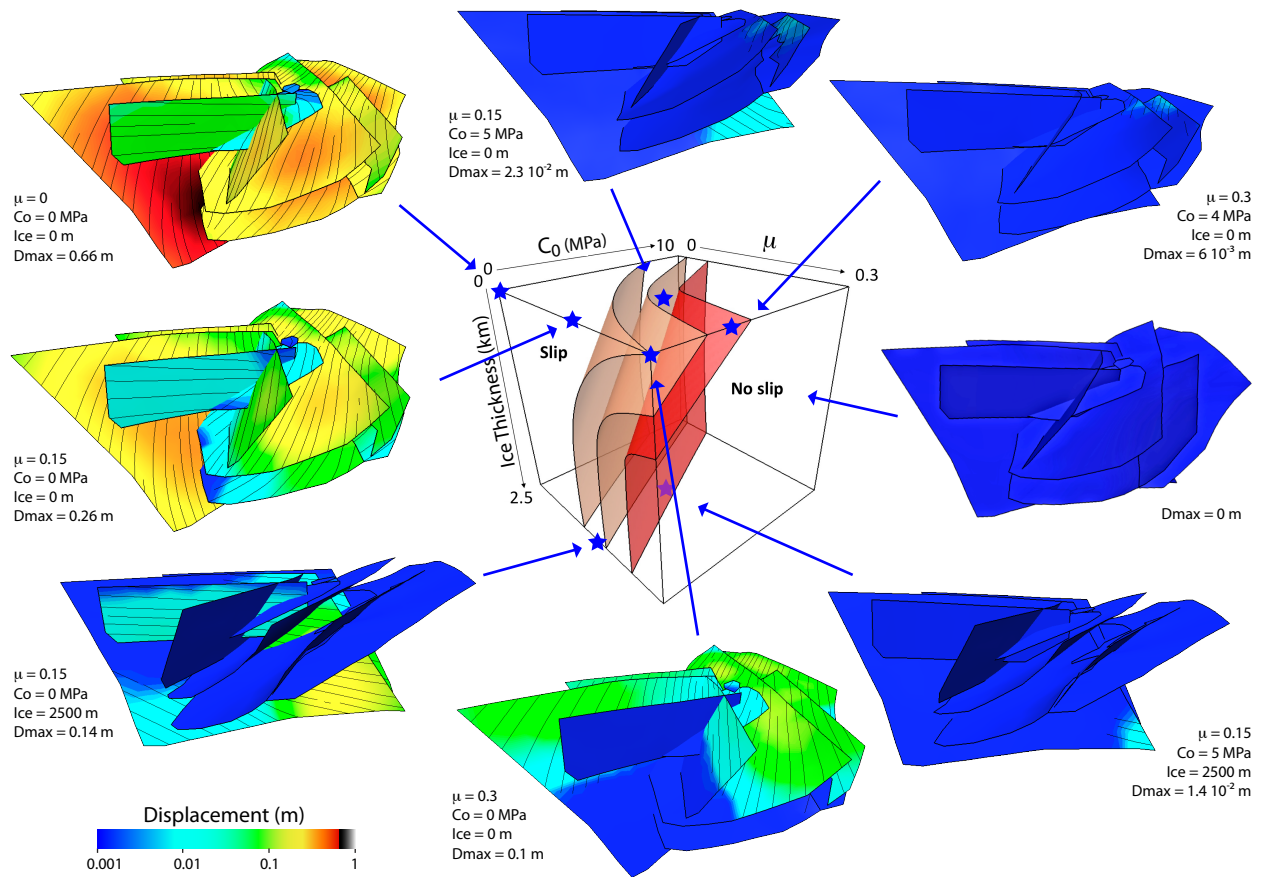
Figure 7

Figure 7 (2 column fitting image). Examples of 3D quasi-static fault displacement distribution on the Olkiluoto model for different loading and fault properties conditions indicated on the fault slip diagram by blue stars. Stream lines on fault surfaces are slickenlines. The colour bar scale for displacement is logarithmic.